Acta Materialia 142 (2018) 58–70

Contents lists available at ScienceDirect

Acta Materialia

journal homepage: www.elsevier.com/locate/actamat

Full length article

Effect of plastic anisotropy on the deformation behavior of bicrystalline aluminum films – Experiments and modeling

Ehsan Izadi, Saul Opie, Harn Lim, Pedro Peralta, Jagannathan Rajagopalan*

Mechanical and Aerospace Engineering, School for Engineering of Matter, Transport and Energy, Arizona State University, Tempe, AZ 85287, USA

ARTICLE INFO

Article history:
Received 1 June 2017
Received in revised form
12 September 2017
Accepted 17 September 2017
Available online 20 September 2017

Keywords:
Strain rate sensitivity
Plastic anisotropy
Bauschinger effect
Thin films
Strain hardening

ABSTRACT

We investigated the effect of texture-induced plastic anisotropy on the deformation behavior of ultrafine-grained aluminum films with a bicrystalline texture (two grain variants). The films were uniaxially loaded along two different directions such that the heterogeneity in the plastic behavior of the two grain variants due to plastic anisotropy was minimized along one direction and maximized along the other. The bicrystalline films show smaller strain rate sensitivity and hysteresis of stress-strain response when they are deformed along the direction that minimizes plastic heterogeneity compared to the direction that maximizes it. Notable differences in flow stress and residual hardening were also found for the two loading directions. To quantitatively understand the effect of plastic anisotropy, we simulated the response of the films using three-dimensional finite elements with a microstructurally explicit model built from TEM automated crystal orientation mapping of the samples that includes a grain boundary region, along with crystal plasticity and anisotropic elasticity. The simulations reveal markedly different distribution of stresses and strains in the two grain variants when loading is performed along the two directions, which can be directly related to the ratio of Schmid factors of their most active slip systems.

1. Introduction

The processing and characterization of ultrafine-grained (UFG) and nanocrystalline (NC) metals and alloys have attracted significant attention in recent years [1,2], because of their superior mechanical properties such as high strength, enhanced corrosion resistance and improved fatigue strength compared to coarse-grained (CG) materials [1,3–6]. In addition, UFG/NC metals exhibit certain unusual characteristics as compared to their CG counterparts, like high strain rate sensitivity, plastic strain recovery and early Bauschinger effect (BE), which have been attributed to changes in the underlying deformation mechanisms [7–13]. Initial research on the deformation behavior of UFG/NC metals focused mainly on the effect of mean grain size on strength and ductility, and the validity of the Hall–Petch relation [14,15], in the UFG/NC regime. Later studies have explored in detail the effect of sample dimensions as well as other microstructural parameters on the flow stress, strain hardening behavior and strain rate sensitivity [16–21]. There has also been a substantial effort to characterize and improve the mechanical and thermal stability of UFG/NC microstructures [22–24].

More recently, texture has been shown to significantly influence the mechanical response of thin UFG/NC metal films [25]. Torre et al. have reported that NC Ni foils with different textures show a variation in the yield stress and ultimate strength [26]. UFG Al films with different textures but similar thickness and mean grain size show substantial changes in BE, and strain rate sensitivity of flow stress [7,27,28]. However, the effect of plastic anisotropy on the deformation behavior of UFG/NC metal films has received relatively little attention. Plastic anisotropy, which can be induced in UFG/NC films as a result of crystallographic texture, can affect the hardening behavior and stress distribution in the grains and influence the extent of inelastic strain recovery. While some studies have considered the effect of Schmid factor variation [25,29–32] on the stress-strain response of both CG and UFG/NC materials, a systematic study of these effects on UFG metal films has been lacking.

To address this issue, we performed monotonic deformation experiments at different strain rates and quasi-static cyclic loading experiments on two sets of UFG aluminum films with identical bicrystalline texture (two grain variants). The films were uniaxially loaded in two different directions with respect to the main crystallographic axes of the bicrystalline texture, such that the

* Corresponding author.
E-mail address: jrajago1@asu.edu (J. Rajagopalan).

https://doi.org/10.1016/j.actamat.2017.09.038
1359-6454/

heterogeneity in the plastic behavior of the two grain variants due to plastic anisotropy was minimized along one direction and maximized along the other direction. The bicrystalline films showed ~20% lower strain rate sensitivity (SRS) when loaded along the direction that minimizes heterogeneity due to plastic anisotropy compared to loading along the direction that maximizes the effect. Cyclic loading-unloading experiments also show significantly less hysteresis in the stress-strain response when the loading is performed along the direction that minimizes heterogeneity due to plastic anisotropy.

To quantitatively understand the effect of plastic anisotropy, we simulated the response of the films using three-dimensional finite elements with a microstructurally explicit model built from automated crystal orientation mapping of the samples along with crystal plasticity and anisotropic elasticity. The simulations quantitatively predict the macroscopic response of the bicrystalline films and provide insights into the evolution of plastic anisotropy-induced stress heterogeneities within the two grain variants, as well as the potential role of the compliance at the grain boundaries.

2. Experimental details

2.1. Thin film synthesis

Two bicrystalline aluminum films (240 nm and 180 nm thick) were deposited on Si (100) wafers using DC magnetron sputtering. The native silicon dioxide layer on the Si wafers was removed through hydrofluoric acid etching and the wafers were immediately transferred to the sputtering chamber (AJA International) to avoid regrowth of the oxide layer. The sputtering chamber was evacuated to a base pressure of $\sim 10^{-7}$ Torr prior to deposition and both films were deposited at a rate of 5.5 nm/min. The Al films grew in a heteroepitaxial manner with the following orientation relationship: Al(110)//Si(001), Al[001]//Si[$1\bar{1}0$] and Al(110)//Si(001), Al [001]//Si[110] [33], leading to two grain families with (110) out-of-plane texture that are rotated 90° in-plane with respect to each other.

2.2. Microstructural characterization and sample fabrication

The microstructures of the films were examined through bright-field transmission electron microscopy (TEM) and automated crystal orientation mapping (ACOM) in the TEM (ACOM-TEM). For the ACOM-TEM measurements, an electron probe with ~1 nm diameter was generated using spot size 4 and 10 μm C2 aperture in a JEOL 200 F ARM TEM. Spot diffraction patterns were obtained from the samples with a 10 nm step size using an electron beam precession angle of 0.4° and a camera length of 120 mm. The acquired ACOM-TEM data was indexed by matching the spot diffraction patterns with a bank of templates for aluminum using the Nanomegas ASTAR™ software package to generate the grain orientation maps. Fig. 1 shows bright-field TEM images of the two Al films, indicating a columnar grain structure. The 180 nm thick film had a mean grain size of 228 nm, whereas the 240 nm thick film had a mean grain size of 275 nm. Selected area diffraction (SAD) patterns taken along the [110]-zone axis (Fig. 2a) showed that only two grain variants, which can be obtained by a 90° rotation with respect to each other in-plane, were present in the films. A schematic representation of these variants is shown in Fig. 2b. The (110) out-of-plane texture and the bicrystalline microstructure of the films were also confirmed by ACOM-TEM measurements (Fig. 2c and d).

After the films were deposited, dog-bone shaped freestanding samples were co-fabricated with a micro-electro-mechanical-system (MEMS) based tensile testing device (Fig. 3a) using microfabrication techniques outlined in Ref. [34]. A piezoelectric actuator (Physik Instrumente) was used to load the MEMS device and a CMOS camera (Thor Labs) was used to acquire optical images of the gauges, G1, G2 and G3, in the device. The force and deformation on the sample during the cyclic loading experiments were obtained by measuring the displacement of the gauges using a custom MATLAB™ program, which tracks prescribed features across a series of images using cross-correlation techniques. The displacement of G1 with respect to G2 ($\Delta X_{12} = X_{G1} - X_{G2}$) represents the deformation of the sample, from which the sample strain is obtained. The deflection of the force-sensing beams is given by the displacement of G2 with respect to G3 ($\Delta X_{23} = X_{G2} - X_{G3}$). As evident from the equivalent mechanical model of the device, the sample is arranged in series with the force-sensing beams (Fig. 3b) and, hence the force on sample and the force-sensing beams is the same. The stiffness of the force-sensing beams (K) was measured in a separate experiment after the sample had fractured. K multiplied by ΔX_{23} gives the force and, thus, the stress on the sample. For measuring the stress-strain response during monotonic loading experiments at different strain rates, a slightly modified MEMS device along with an external micro load cell was used, as described in Ref. [27].

To determine the error in strain measurement, we displaced the gauges by a prescribed amount and recorded images before and

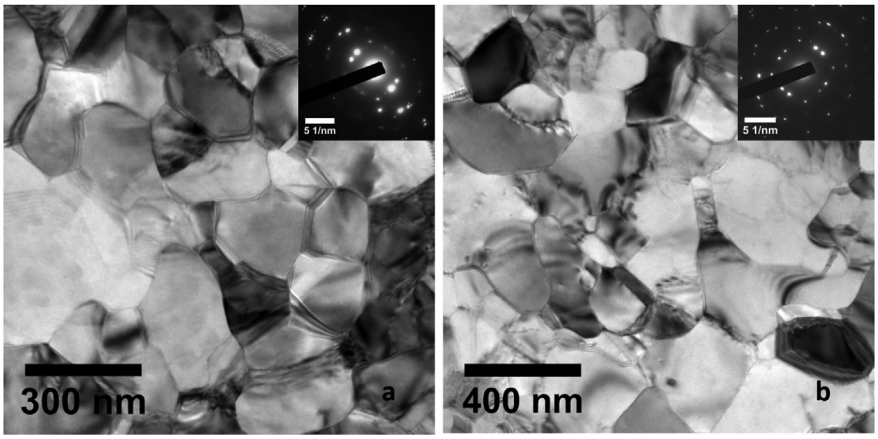

Fig. 1. (a) Bright-field TEM image of a 180 nm thick, bicrystalline aluminum film with a mean grain size of 228 nm. (b) Bright-field TEM image of a 240 nm thick, bicrystalline aluminum film with a mean grain size of 275 nm. The selected area diffraction (SAD) patterns for both films (insets in (a) and (b)) show the (110) out of plane texture. The two in-plane variants that can be obtained by a 90° rotation with respect to each other about the out-of-plane direction.

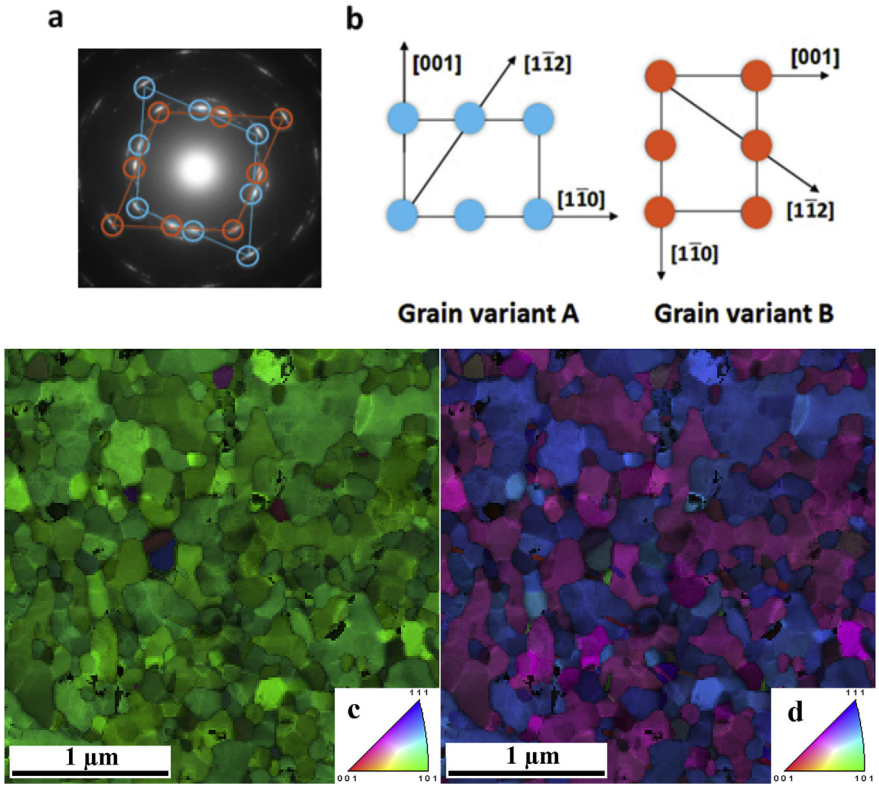

Fig. 2. (a) Diffraction pattern of the bicrystalline film, showing the spots (blue and red circles) from the two-grain variants. (b) Schematic representation of the two variants and their corresponding crystal directions. (c) Inverse pole figure map from one of the films with colors showing crystal orientations perpendicular to the film (color key for crystal directions is shown in the standard triangle legend) (d) Inverse pole figure map of the same area as (c), but with colors corresponding to crystal axes parallel to the horizontal direction. The colors in (c) clearly show the strong (110) out-of-plane texture. (For interpretation of the references to colour in this figure legend, the reader is referred to the web version of this article.)

after displacement. We then analyzed the images using the MATLAB™ based image-processing technique and calculated the displacement of the gauges. By comparing the calculated displacement with the imposed displacement, we determined the accuracy of the displacement measurement to be ~13 nm, which translates to a strain accuracy of ~3.5×10^{-5}. We also determined the uncertainty in the measured stress, which comes from two sources – the variation in sample thickness and the error in the force measurement. The variation in sample thickness (cross-sectional area) is ~ 1–2%, which translates to an uncertainty of 3–7 MPa in the calculated stress. In addition, there is an approximately 5 μN error in the force measurement, which leads to an additional error of ~3 MPa. As a result, the combined uncertainty in the stress measurement is ~10 MPa. Both the Al films were under compressive stress in the as-deposited state and, therefore, the freestanding samples buckled when they were released from the Si

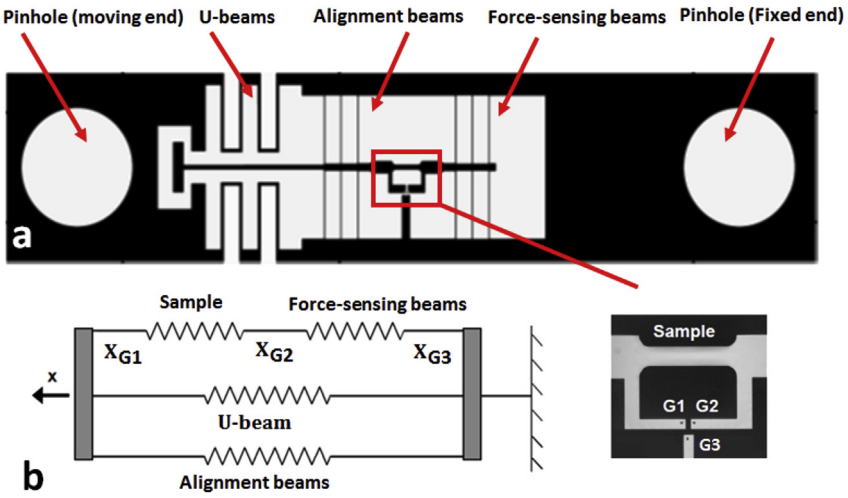

Fig. 3. a) MEMS device for performing tensile experiments on freestanding metal film samples. The nominal strain on the sample is obtained by tracking the displacement of gauges G1 and G2. b) Equivalent mechanical model of the MEMS device. The U-beams and Alignment beams are in parallel with the sample and hence their displacement (x) is the same.

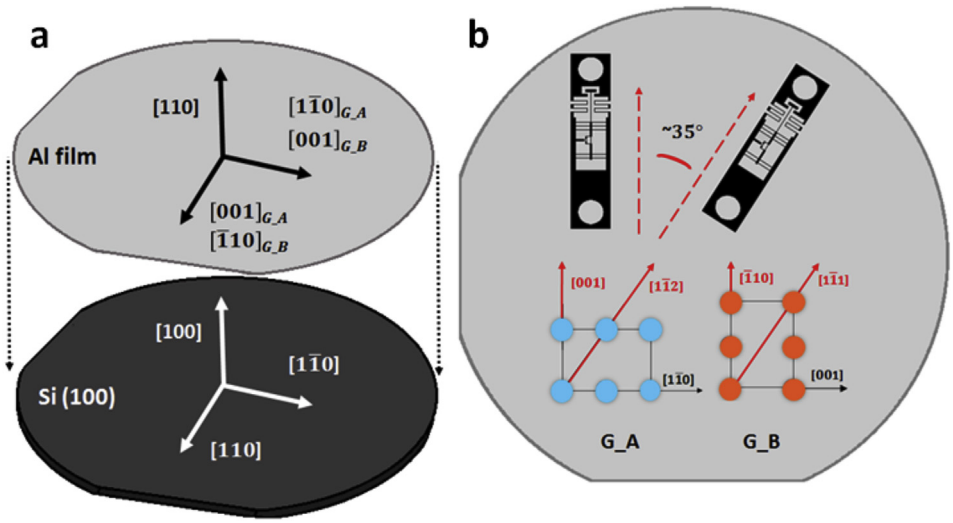

Fig. 4. a) Schematic showing the epitaxial relationship between the Si substrate and the Al film. b) Orientation of the devices for loading the film along the two different directions ($[001]_{G\_A}$ and $[1\bar{1}2]_{G\_A}$).

substrate. However, the samples were almost macroscopically stress-free before loading since the stress for buckling along the length is very low (<0.5 MPa).

The MEMS devices were fabricated along two different orientations as illustrated in Fig. 4 to allow loading of the samples along the [001] and $[1\bar{1}2]$ directions of the grain variant A in the bicrystalline films. From here on, these directions are referred to as $[001]_{G\_A}$ and $[1\bar{1}2]_{G\_A}$, respectively. The [001] and $[1\bar{1}2]$ directions of the grain variant A coincide with the $[\bar{1}10]$ and $[1\bar{1}1]$ directions, respectively, of the grain variant B. When the loading is along $[001]_{G\_A}$, there are eight active slip systems in grain variant A and four active slip systems in grain variant B. The Schmid factor (s) of all the active slip systems, in both the grain variants, is identical ($s = 0.408$); hence, this loading direction minimizes heterogeneity due to plastic anisotropy. In contrast, for loading along $[1\bar{1}2]_{G\_A}$, two slip systems, $\{111\}$ $[0\bar{1}1]$ and $\{1\bar{1}1\}$ $[\bar{1}\bar{1}0]$, of grain variant A have $s = 0.408$, whereas the maximum Schmid factor in grain variant B is only 0.272, leading to large heterogeneity due to plastic anisotropy.

Since this study is intended to isolate the effect of plastic anisotropy on the deformation behavior of UFG Al films it is necessary to minimize other factors that could alter the mechanical response. Therefore, in addition to the mean grain size, the specimen width (75 μm) and length (375 μm) were kept constant for all experiments. To ensure the repeatability of the observations, at least two specimens were tested for each experimental condition.

2.3. Experiments

The mechanical behavior of the bicrystalline Al films was investigated through monotonic and cyclic load-unload tensile experiments along $[001]_{G\_A}$ and $[1\bar{1}2]_{G\_A}$ loading directions. The monotonic loading experiments were conducted on the 240 nm thick aluminum film at strain rates ranging from ~7×10^{-6} s^{-1} to 7×10^{-3} s^{-1}. The details of the procedure adopted for the strain rate experiments can be found in Ref. [27]. We chose the stress at 0.9% strain ($\sigma_{0.9\%}$) as a measure of flow stress to quantitatively compare the response at different rates. The flow stress at 0.9% strain was chosen because macroscopic plasticity had set in before 0.9% strain and the samples failed around 1% strain at higher strain rates. The cyclic load-unload experiments were conducted on the 180 nm thick Al film at a strain rate of ~10^{-5} s^{-1}. The specimens were subjected to two deformation cycles before they fractured during the third loading.

2.4. Crystal plasticity model

The simple analysis based on the Schmid factor offered above assumes that the state of stress inside each variant is approximately uniaxial, which is likely to be a reasonable assumption for strains within the elastic regime, given the low elastic anisotropy of pure Al [35]. However, within the plastic regime, plastic strain tensors produced by dislocation slip can change due to the effect of crystal orientation on slip geometry, potentially leading to different levels of interaction between the two grain variants for the two loading directions used. Therefore, several simulations were performed, first with a homogenized model based on polycrystalline plasticity via the Taylor model and then with microstructurally explicit models using the well-known strain hardening formulation described by Asaro in Ref. [36], and a non-linear kinematic hardening rule with linear dynamic recovery for each slip system, similar to that shown in Ref. [37]. Note that the crystal plasticity kinematics in this formulation allows for crystal rotation with plastic deformation (e.g., [38]). Furthermore, the microstructurally explicit models were also augmented to account explicitly for the presence of a grain boundary region with higher plastic compliance compared to the bulk, i.e., a composite model, as described in Ref. [39] and references therein. An elastic-perfectly plastic model was chosen for the grain boundary phase to keep the model as simple as possible. The simulations allowed us to quantify the states of stress and strain within each variant and the grain boundary region for both loading directions. Furthermore, the simulations helped us understand the connections between plastic anisotropy and both local and global behavior during monotonic tensile experiments as well as cyclic load-unload experiments.

The calibration of material parameters for the simulation followed a sequential procedure where the simplest models were used first and then additional physics was incorporated if constraints from experimental results could not be met. In that regard, models were first calibrated to match the experimental data obtained from the quasi-static cycling loading experiments along the $[001]_{G\_A}$ direction. Key parameters from the experiments that were chosen to match with the simulations include the flow stresses before each unloading, the unloading slopes, the residual strains at

zero load after each unloading and the loading-unloading hysteresis. A Taylor model with just crystal plasticity and kinematic hardening was first used to get initial values of the material parameters. Then microstructurally explicitly models were used, first without grain boundary regions and then with grain boundary phase added as needed. Those parameters were then used to *predict* the behavior for monotonic loading along $[001]_{G\_A}$ and $[1\bar{1}2]_{G\_A}$ and the simulation results were compared with the corresponding experimental data for validation. The microstructurally explicit simulations were then used to obtain volume averages of the stresses and strains within each variant, as well as global stress-strain curves for each loading orientation. Finally, shortcomings and potential ways to improve the model, as revealed by the loading-unloading behavior along $[1\bar{1}2]_{G\_A}$ direction, are discussed. The procedure to build the finite element models is described next.

2.4.1. Finite element models

All models were based on a 2000 nm × 2000 nm x 100 nm body, leading to a 20 to 1 aspect ratio (length to thickness and also width to thickness), that should produce the plane stress conditions along the thickness and plane strain conditions along the width that are expected in the actual samples. The mesh for the Taylor model consisted of 100 nm hexahedral elements. The microstructurally explicit model was created using either geometry obtained from the ACOM-TEM data or by using Voronoi tessellations with the same average grain size and grain orientations as that determined from ACOM-TEM data. The tessellations were generated using the add-on tool for ABAQUS™ described in Ref. [40], while variants were assigned by hand following results from ACOM-TEM measurements.

The meshing process based on the ACOM-TEM data started from an inverse pole figure map similar to that shown in Fig. 2d, which was used to recreate a three-dimensional columnar microstructure by extruding this geometry along the 100 nm (thickness) direction, with regions corresponding to each variant segmented and interpolated using AvizoFire™ software. Then, a fine tetrahedral mesh was used to discretize the 3-D geometry and reproduce the smooth boundaries between the grains. The resulting mesh had ~585 k elements, which was considered fine enough to ensure

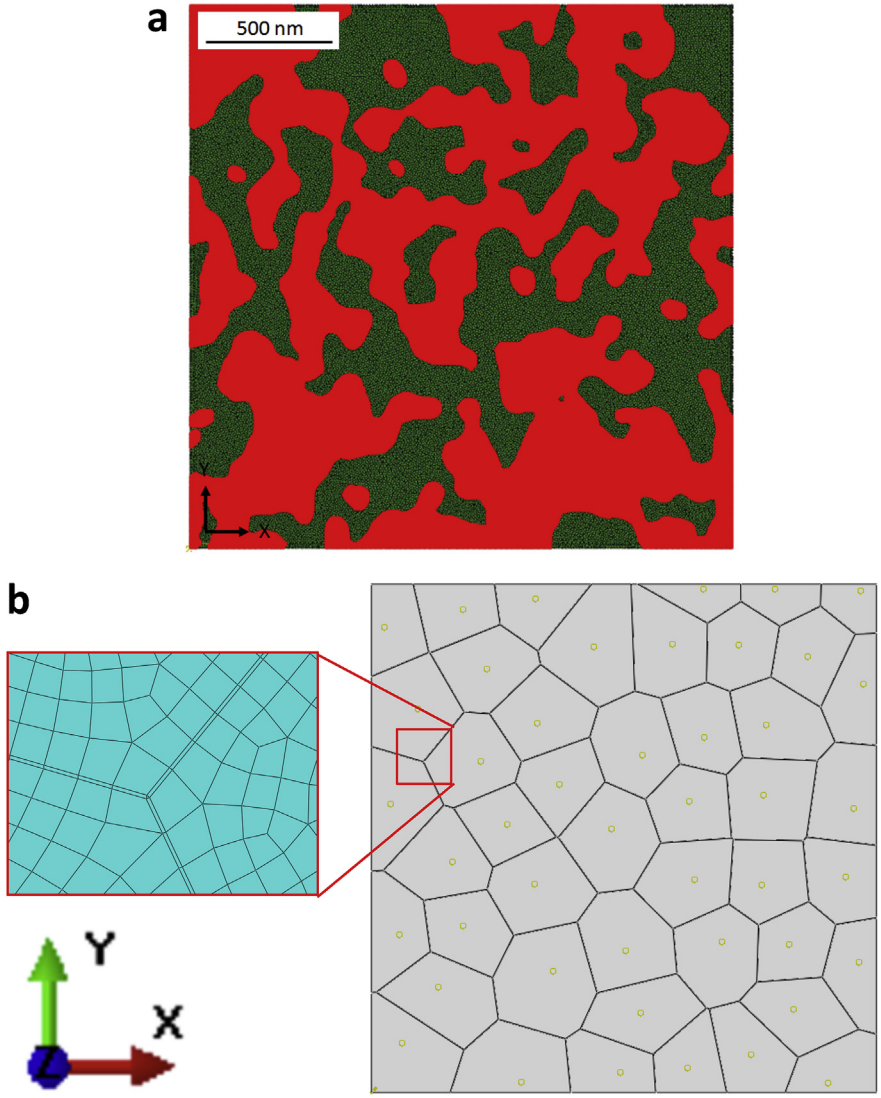

Fig. 5. Plan views of the meshes used for the microstructurally explicit simulation (a) geometry obtained from ACOM-TEM data and AvizoFire™. The red region is grain variant A. (b) Geometry obtained from a Voronoi tessellation including detail of the grain boundary region. (For interpretation of the references to colour in this figure legend, the reader is referred to the web version of this article.)

convergence of the numerical simulation. The procedure to create meshes from the Voronoi tessellation was similar, except that hexahedral elements were used for grain interiors. When the grain boundary phase was included, hexahedral elements were used for the boundary as well, except at triple junctions, where wedge elements were utilized. The thickness of the grain boundary layer was kept at about 1/200 of the grain diameter and this resulted in volume fractions of 50.93% for variant A, 47.94% for variant B and 1.13% for the grain boundary region. Examples of resulting models are shown in Fig. 5.

All models were constrained to replicate pure tension, i.e., one face was constrained to stop motion along the loading direction (Y axis), and then either one node on that face was fully constrained, or a face normal to the X (or Z) axis was constrained to stop X (or Z) movement. The latter constraints were used due to the former introducing some minor twisting in the microstructurally explicit model due to anisotropy on the two variants. All out of plane constraints were such that the conditions of plane stress perpendicular to the thickness of the films were maintained. All models were loaded along the Y direction, via an applied displacement on the face opposite to the one being constrained, at a strain rate of 10^{-3} s^{-1}, e.g., a ramp displacement up to a maximum value of 40 nm over 20 s, to a final total strain of about 2%, although most simulations were performed to lower total strains (~1.5%), while keeping the same strain rate. Appropriate histories based on the experiments were used for the quasi-static cyclic simulations. All models were analyzed with the implicit ABAQUS™/Standard solver using a user defined material subroutine (UMAT).

3. Results

3.1. Strain-rate experiments

Fig. 6 shows the stress-strain response of the 240 nm Al film, loaded along $[001]_{G\_A}$ and $[1\bar{1}2]_{G\_A}$, respectively, at different strain rates. The data show an initial linear elastic region for both loading directions, where the curves at different strain rates are nearly identical. It is noted that the initial stress-strain slope for both the loading directions is less than the bulk Young's modulus of Al ($E = 69$ GPa) for reasons explained in Ref. [27].

As evident from Fig. 6a the stress-strain curves of the 240 nm thick bicrystalline film loaded along $[001]_{G\_A}$ showed very little variation across different strain rates, except at the highest strain rate. In contrast, when loaded along $[1\bar{1}2]_{G\_A}$ the same film exhibited a more perceptible strain rate effect (Fig. 6b). As a result, the strain rate sensitivity exponent ($m = dlog(\sigma)/dlog(\dot{\varepsilon})$) was ~20% lower for loading along $[001]_{G\_A}$ ($m = 0.017 \pm 0.007$) compared to $[1\bar{1}2]_{G\_A}$ ($m = 0.021 \pm 0.002$), as shown in Fig. 6c. In addition, the stress required to induce macroscopic plasticity was higher for loading along $[1\bar{1}2]_{G\_A}$ compared to $[001]_{G\_A}$. Thus, for a given strain and strain rate, the stress was higher for loading along $[1\bar{1}2]_{G\_A}$ compared to $[001]_{G\_A}$.

3.2. Quasi-static cyclic loading experiments

The cyclic load-unload experiments along $[1\bar{1}2]_{G\_A}$ and $[001]_{G\_A}$ directions of the 180 nm thick film also revealed two notable differences in behavior (Fig. 7). First, the deviation from elastic behavior during unloading was larger for the $[1\bar{1}2]_{G\_A}$ loading direction, leading to a larger hysteresis (ε_h, see Fig. 7a) in the stress-strain response. While the normalized hysteresis strain ($\varepsilon_h/\varepsilon_p$) for $[1\bar{1}2]_{G\_A}$ loading was only slightly higher compared to $[001]_{G\_A}$ loading for the first cycle (Table 1), $\varepsilon_h/\varepsilon_p$ decreased significantly for

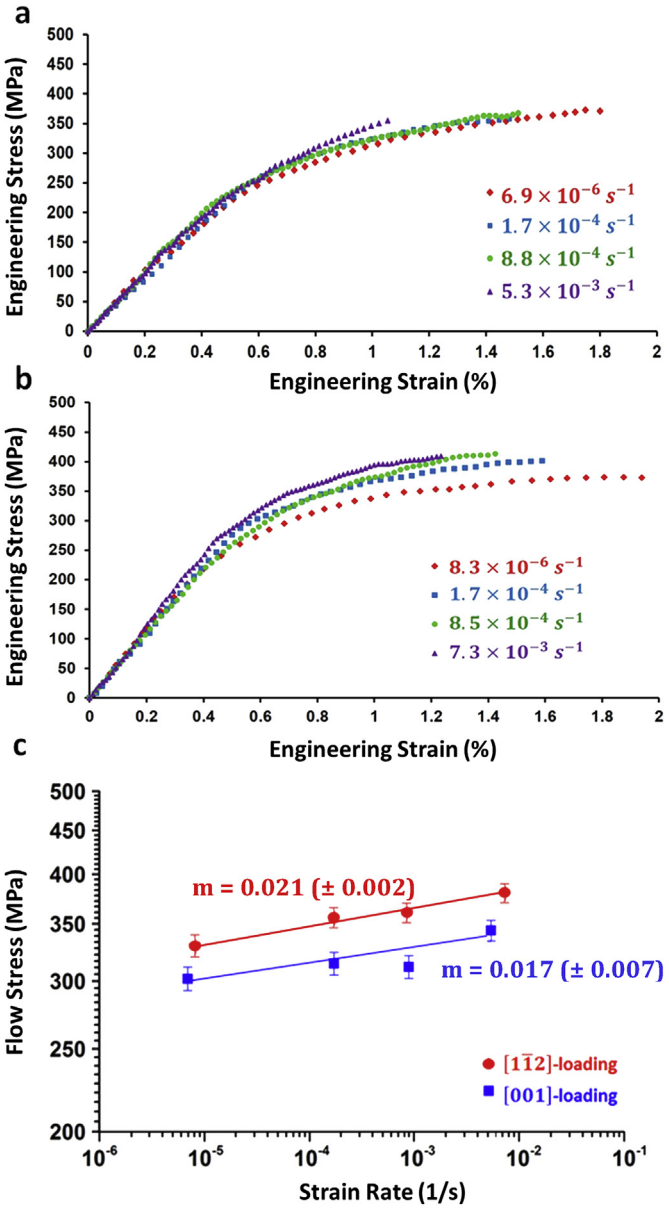

Fig. 6. (a) Stress-strain response of the Al 240 nm film for $[001]_{G\_A}$ loading at different strain rates. (b) Stress-strain response of the Al 240 nm film for $[1\bar{1}2]_{G\_A}$ loading at different strain rates. (c) Log-log plot of flow stress versus strain rate for the two loading directions. The error bars indicate the bounds of uncertainty in flow stress arising from both film thickness variation and load cell fluctuations. The value in brackets for 'm' correspond to the standard error.

$[001]_{G\_A}$ loading during the second cycle. As a result, $\varepsilon_h/\varepsilon_p$ for $[1\bar{1}2]_{G\_A}$ loading was more than 30% higher compared to $[001]_{G\_A}$ loading during the second cycle.

Second, the stress for a given strain was lower for the $[001]_{G\_A}$ loading direction compared to the $[1\bar{1}2]_{G\_A}$ loading direction during the first cycle (Fig. 7b). However, the residual hardening was higher for the $[001]_{G\_A}$ loading direction, which diminished the stress difference in the subsequent cycles. For instance, $\sigma_{0.8\%}$ was ~350 MPa for $[001]_{G\_A}$ loading during the first cycle, whereas it was ~380 MPa for $[1\bar{1}2]_{G\_A}$ loading, a difference of 30 MPa. By the third cycle, the difference in $\sigma_{0.8\%}$ reduced to 15 MPa (415 MPa for $[001]_{G\_A}$ loading, 430 MPa for $[1\bar{1}2]_{G\_A}$ loading).

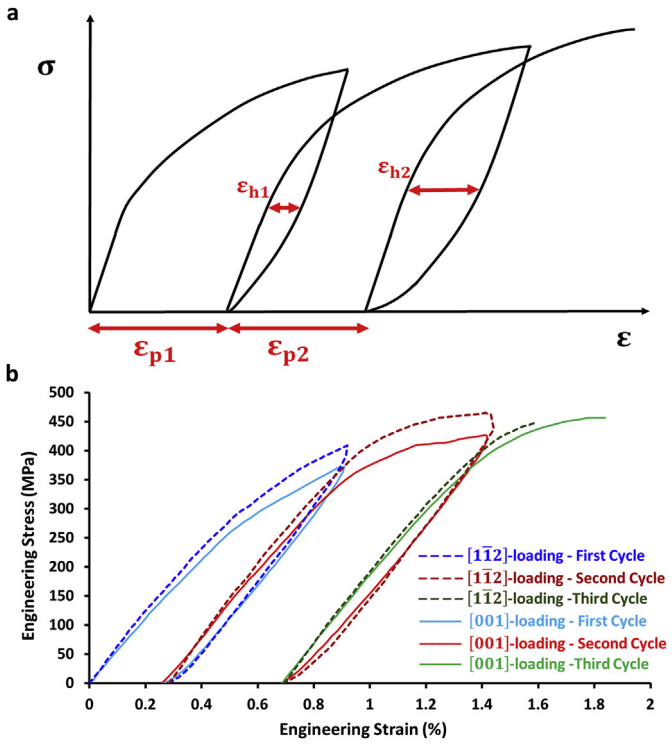

Fig. 7. (a) Schematic of stress-strain response of bicrystalline Al films during cyclic load-unload experiments. (b) Stress-strain response of the 180 nm thick Al film for loading along the $[001]_{G\_A}$ direction and $[1\bar{1}2]_{G\_A}$ direction.

3.3. Crystal plasticity results

Material parameters were varied for both the Taylor and microstructurally explicit simulations. Equations (1)–(5) below, describe the basic flow rule and hardening laws implemented in the UMAT used here.

$$\dot{\gamma}^{\alpha} = \dot{\gamma}_0 \left| \frac{\tau_r^{\alpha} - \chi^{\alpha}}{\tau_c^{\alpha}} \right|^{\frac{1}{m}} sign(\tau_r^{\alpha} - \chi^{\alpha}) \tag{1}$$

$$\dot{\tau}_c^{\alpha} = \sum_{\beta=1}^{N} h_{\alpha\beta} \left| \dot{\gamma}^{\beta} \right| \tag{2}$$

$$h_{\alpha\alpha} = h(\gamma) = h_0 \mathrm{sech}^2 \left(\frac{h_0 \gamma}{\tau_s - \tau_0} \right), \quad h_{\alpha\beta} = q h(\gamma)\ \alpha \neq \beta \tag{3}$$

$$\gamma = \sum_{\alpha=1}^{N} \int |\dot{\gamma}^{\alpha}| dt \tag{4}$$

$$\dot{\chi}^{\alpha} = k_1 \dot{\gamma}^{\alpha} - k_2 |\dot{\gamma}^{\alpha}| \tag{5}$$

where $\dot{\gamma}^{\alpha}$ is the plastic shear strain rate in slip system α, $\dot{\gamma}_0$ is a reference shear strain rate, τ_r^{α} is the resolved shear stress for slip system α, χ^{α} is the backstress on slip system α, τ_c^{α} is the current critical resolved shear stress needed to produce dislocation motion in the slip system α (flow shear strength), m is the strain rate sensitivity, $\dot{\tau}_c^{\alpha}$ is the hardening rate for the shear strength in the slip system α, $h_{\alpha\beta}$ is the hardening matrix, h_0 is the initial hardening rate, τ_0 is the initial shear yield strength, τ_s is the stage I shear strength [36], q is the latent hardening ratio, $\dot{\chi}^{\alpha}$ is the rate of change of the backstress on slip system α, and k_1 and k_2 are constants.

The power-law used in equation (1) for the plastic shear strain rate is a very commonly used form [36] that tends to work fairly well, whereas equations (2) and (3) imply that hardening takes place due to both slip activity on a system and by slip activity on others, i.e., both self and latent hardening occur, which allows slip systems to harden at different rates.

As mentioned above, the results from the quasi-static cyclic loading experiments along $[001]_{G\_A}$ were used to start the calibration process for the material parameters, using a Taylor model, i.e., assuming the same total strain for each variant, along with the crystal plasticity model described in equation (1) through (5), without using a grain boundary phase. The Taylor simulations took less than a minute and provided an initial estimate of the single crystal parameters. It was noticed quickly that many of the parameters from the experimental curves that were selected for matching could not be replicated by pure kinematic hardening alone using the Taylor assumption.

A microstructurally explicit model was then used, and although it produced better matches than the Taylor model, it could not reproduce the loading-unloading hysteresis seen in the experiments. Finally, a grain boundary phase was introduced in the model that led to considerable improvement in the matching with the experimental data, including the hysteresis. Furthermore, through a systematic variation of the parameters it was found that lowering the values of k_1 and k_2 led to better agreement with the experiments. Given that the literature suggests that macroscopic kinematic hardening effects, including hysteresis, can arise due to interactions between phases/grains with different properties in both polycrystalline [37] and NC materials [7], the kinematic hardening portion of the model was completely suppressed ($k_1 = k_2 = 0$), and the matching was done purely by changing the parameters used in equation (1) though (3) as well as the properties of the grain boundary phase. Table 2 lists the parameters that led to the best match obtained with the microstructurally explicit model including a grain boundary phase. Note that the anisotropic elastic constants for the Al grains C11, C12 and C44 were obtained from the literature [41].

Fig. 8 shows the results of the microstructurally explicit model (with self and latent hardening) that included a grain boundary

Table 1
Hysteresis strain during the cyclic deformation of the 180 nm thick Al film along the two directions.

	ε_{h1} (%)	ε_{h2} (%)	$\frac{\varepsilon_{h1}}{\varepsilon_{p1}}$	$\frac{\varepsilon_{h2}}{\varepsilon_{p2}}$
$[001]_{G\_A}$ loading	0.0503	0.0616	0.1941	0.1441
$[1\bar{1}2]_{G\_A}$ loading	0.0559	0.0791	0.1977	0.1926

Table 2
Material parameters used in simulations.

Crystal Plasticity	Value
Reference Slip Rate, $\dot{\gamma}_0^{\alpha}$ [1/s]	0.001
Strain Rate Sensitivity, m [-]	0.02
Initial Hardening Rate, h_0 [MPa]	8.0e3
Initial Critical Resolved Shear Stress, τ_0 [MPa]	150.0
Stage I shear strength, τ_s [MPa]	250.0
Latent hardening ratio, q	1.0
C11, [GPa]	108.2
C12, [GPa]	61.3
C44, [GPa]	28.5
Grain Boundary Region	
Sy [MPa]	70.0
Young's Modulus [GPa]	70.0
Poisson's ratio	0.35

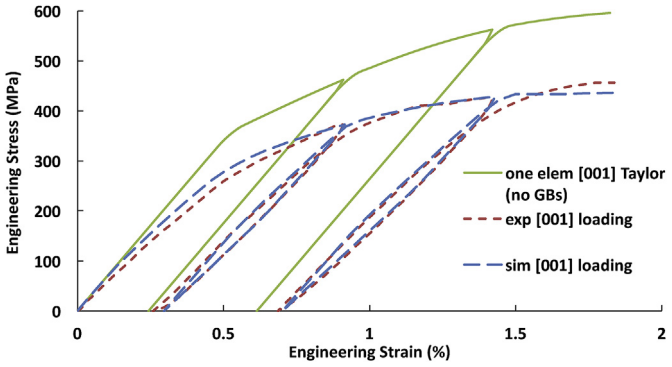

Fig. 8. Comparison between experimental stress - strain curves and predictions (σ_{yy} vs ε_{yy}) from the Taylor and microstructurally explicit models for quasi-static cyclic loading along $[001]_{G\_A}$.

phase and a one element Taylor model (no grain boundaries) without intrinsic backstress for comparison along with the experimental data. Both models used the same crystal plasticity material parameters for the bulk. As evident from the figure, the Taylor model did not provide a good match with the experiments and could not reproduce the loading-unloading hysteresis. The microstructurally explicit crystal plasticity model (with grain boundary phase) led to excellent quantitative agreement between the experimental data and the simulation results. This shows that the backstresses in this material are indeed the result of heterogeneity in properties of the grain interiors and grain boundaries, which rendered explicit incorporation of kinematic hardening models unnecessary.

The calibrated model resulting from the procedures described above needed to be validated against experimental data not used for the calibration process. In this case, the model was used to predict stress-strain curves obtained under monotonic loading with a known strain rate for the two loading directions. One issue with this approach is that the films used for the quasi-static cyclic loading experiments, which provided the calibration data, were thinner than those used for monotonic tensile testing, and it is a well-known fact that the yield strength of thin films depends on both film thickness and the grain size [42–44]. Given that both films had a similar bicrystalline microstructure, a thickness correction needed to be applied before using the model on the thicker films. In particular, the yield strength of thin films has been shown to scale with the inverse of the film thickness [42–44], so the values of τ_0 and τ_s were multiplied by $1/(240/180) = 0.75$, for the thicker samples. No other corrections were made. The model predictions for the stress-strain curves after these modifications are shown in Fig. 9, along with the corresponding experimental data. The simulations predict a higher stiffness at low values of stress and strain, which is related to elastic compliance issues associated with sample buckling (see Ref. [27]). However, the agreement improves considerably at higher loads, with good matching for the $[1\bar{1}2]_{G\_A}$ loading and excellent agreement for [001]G_A loading, which is not unexpected given the data used for calibration.

The results from the microstructurally explicit model were used to examine the behavior of each variant. In this regard, volume averages of the stresses and strains in each of them were obtained from the numerical solution and then used to obtain stress-strain curves for each variant along the loading direction. The resulting stress-strain curves for loading along $[001]_{G\_A}$ is shown in Fig. 10, along with contour plots of von Mises stress at 1.5% macroscopic strain.

Note that the individual stress-strain curves in terms of the applied strain for the two variants are quite close, with the stress for variant B, which has a loading axis parallel to [110] in this case, being slightly higher. The von Mises stress exhibits some variability,

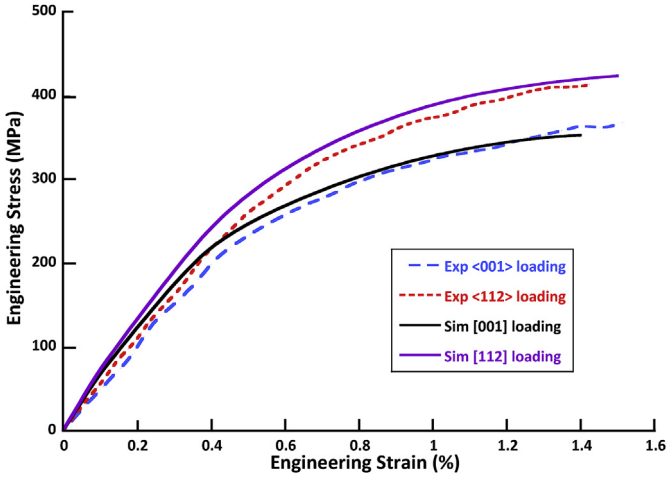

Fig. 9. Comparison between experimental stress - strain curves under monotonic loading and predictions (σ_{yy} vs ε_{yy}) from the microstructurally explicit model for the two loading directions. The experimental data for $[001]_{G\_A}$ loading was obtained at a strain rate of 8.8×10^{-4} s^{-1}, and at 8.5×10^{-4} s^{-1} for $[1\bar{1}2]_{G\_A}$ loading.

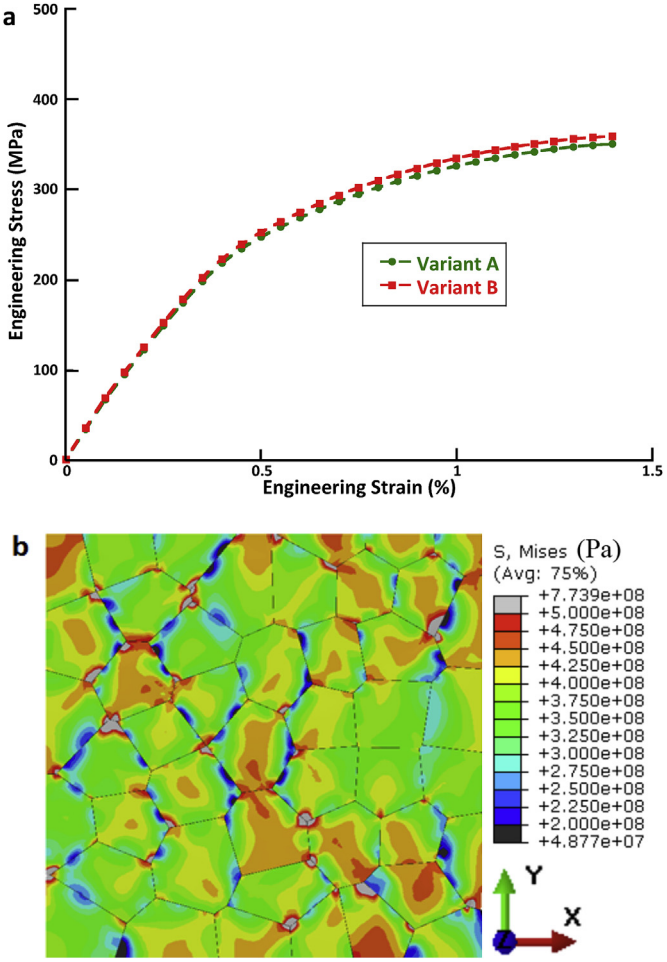

Fig. 10. Local mechanical response from the simulation of monotonic loading along $[001]_{G\_A}$. (a) Volume averaged stress (σ_{yy}) in each variant versus macroscopic strain (ε_{yy}). (b) Von Mises stress distribution at 1.5% macroscopic strain.

with values approximately equal to the applied stress across grains from both variants (green contours at about 350 MPa), but also with values both lower and higher. Note that low values of von Mises stress occur always close to grain boundaries that are highly inclined with respect to the horizonal axis (x-axis, in this case), whereas high values of von Mises stress occur at triple junctions and also at several locations where grain boundaries are almost perpendicular to the loading axis (y-axis). The low values are likely indication of local stress relaxation due to sliding along the softer grain boundaries, which helps maintain the average stresses in both variants about the same. These results indicate that the orientation of the grain boundaries with respect to the load direction is playing a role in the simulation, which, in turn, suggests that additional effects associated with grain boundaries might be present for non-equiaxed microstructures, e.g., elongated grains, where a higher fraction of the GBs might be either parallel or perpendicular to the applied load depending on how samples are loaded. However, the samples used in this study are not likely to be affected by these effects due to the uniform size and shape of their grains.

The results for loading along $[1\bar{1}2]_{G\_A}$ were different from those for loading along $[001]_{G\_A}$, as shown in Fig. 11. The stress-strain curves obtained for the two variants (Fig. 11a) showed that their responses to applied load had larger differences between one another and the macroscopic stress-strain response than for the $[100]_{G\_A}$ loading. Stress partitioning between the two variants for this case is illustrated in Fig. 11b and c, which show the von Mises stress distribution for a 1.5% macroscopic applied strain. Although the stress could be high in either variant, the stress in variant B was found to be higher more often than for variant A. Furthermore, note that the heterogeneity in the stress distribution is much more pronounced than for the $[001]_{G\_A}$ case.

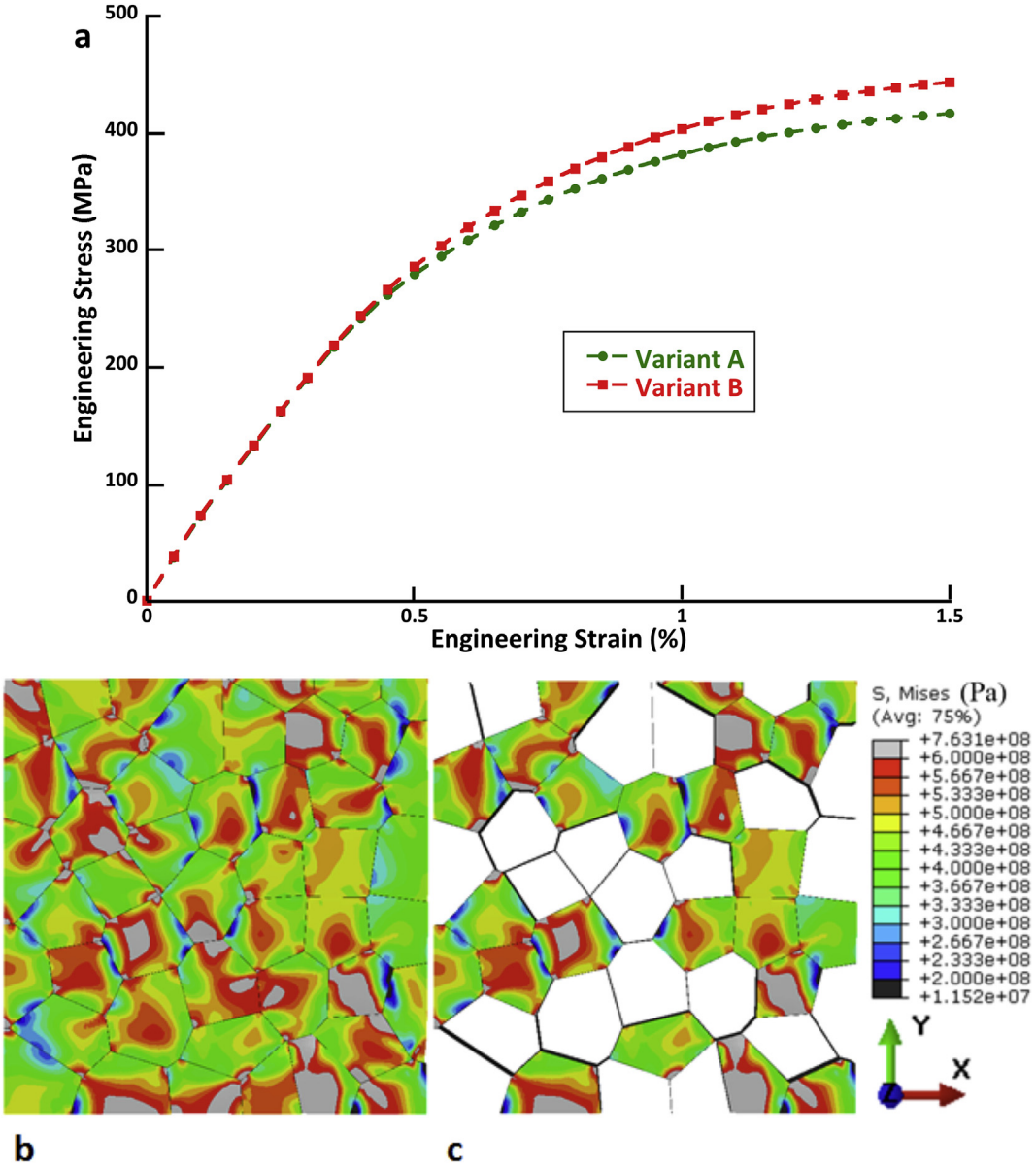

Fig. 11. Local mechanical response from the simulation of monotonic loading along $[1\bar{1}2]_{G\_A}$. (a) Volume averaged stress (σ_{yy}) in each variant versus macroscopic strain (ε_{yy}) (b) von Mises stress at 1.5% macroscopic strain (c) von Mises stress in Variant B at 1.5% macroscopic strain. The color bar applies to both (b) and (c). (For interpretation of the references to colour in this figure legend, the reader is referred to the web version of this article.)

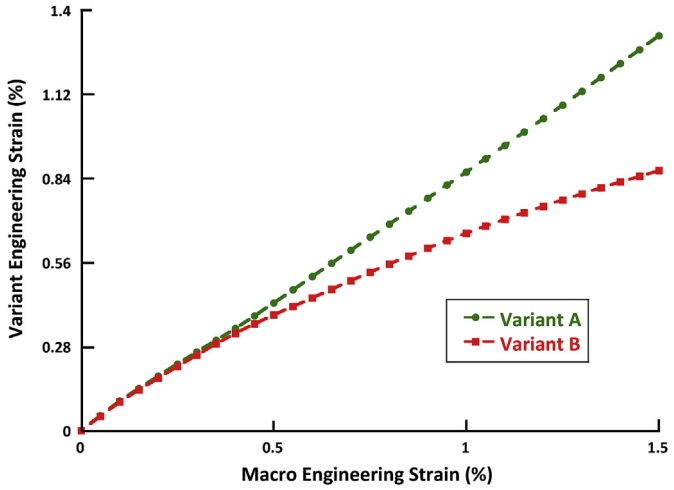

Fig. 12. Volume average of variant strain (ε_{yy}^{var}) versus the macroscopic engineering strain (ε_{yy}) from simulations of monotonic loading along the $[1\bar{1}2]_{G\_A}$ direction.

The average strain response of each variant for the $[1\bar{1}2]_{G\_A}$ case, shown in Fig. 12, indicates that, while strains in both variants are about the same up to a macroscopic strain of 0.2%, their response starts to differ above that value. The plot shows clearly that variant A carried a larger strain than variant B and the way the strain is portioned also indicates that the grain boundary region produces displacements along the load direction that are responsible for a meaningful fraction (~25%) of the macroscopic strain. Simulations suggest that these displacements are mostly due to shear at the grain boundary phase, in a way quite similar to grain boundary sliding. The stresses and strains at the grain boundaries also play a key role on the development of backstresses leading to loading-unloading hysteresis, as described next.

Normal stress along the loading direction in each variant and the grain boundaries as a function of macroscopic strain is shown in Fig. 13 for both loading directions. The plots show trends that agree with those obtained from monotonic loading simulations in terms of how stresses are distributed among variants, i.e., variant B taking more stress than variant A, in both cases, with with results for loading along $[001]_{G\_A}$ (Fig. 13a) being a lot more homogenous than for loading along $[1\bar{1}2]_{G\_A}$. The plots show that the grain boundary phase plays a key role on the development of hysteresis during loading-unloading of the samples for both loading directions, as the hysteresis for the grain boundary phase is much more pronounced than for the individual variants. Furthermore, note that the normal stress in the grain boundary phase becomes negative while the stresses in the variants are still positive. The value of the compressive stress actually increases in absolute value with strain, which means larger backstresses. This, in turn, correlates well with an increase in the hysteresis strain ε_h.

4. Discussion

4.1. Stress-strain response and strain rate sensitivity

In the bicrystalline Al films explored here, the initial stage of deformation is relatively homogeneous because elastic moduli for grain variants A and B along both loading directions are quite similar. The elastic modulus of variant A is 63.7 GPa and variant B is 72.5 GPa for loading along $[001]_{G\_A}$. The corresponding values for $[1\bar{1}2]_{G\_A}$ loading are 71.8 GPa and 75.6 GPa, respectively. Thus, the elastic strain mismatch between the grains is small regardless of the loading direction. However, the plastic behavior is significantly different for the two loading directions. For the $[001]_{G\_A}$ loading direction, heterogeneity in the plastic response due to anisotropy is very small and the local response remains relatively homogeneous even after the film starts to deform plastically, as corroborated by the simulations results shown in Fig. 10. The small differences in stiffness between the two variants for loading along $[001]_{G\_A}$ actually correlate with the slightly higher stress in variant B revealed by the simulations (Fig. 10a). In contrast, for $[1\bar{1}2]_{G\_A}$ loading, heterogeneity in the plastic response is higher as discussed in section 2.2. As a result, there is considerable plastic strain mismatch between adjoining grains, as shown in Fig. 12, and the grains need to rotate with respect to each other to maintain strain compatibility. Such grain rotations have been shown to be time dependent [27,45], which leads to a higher strain rate sensitivity for loading along $[1\bar{1}2]_{G\_A}$ direction.

A potential mechanism to explain and model the rate dependence of these grain rotations is the sliding-like deformation of the GB phase described in the previous section. When the GB phase shears, the interior of the grain is likely to "follow" this shear via a rigid body-like rotation, which would translate to a change in grain orientation during *in situ* TEM observations. The amount of rotation would be related to the amount of GB deformation, which, in turn,

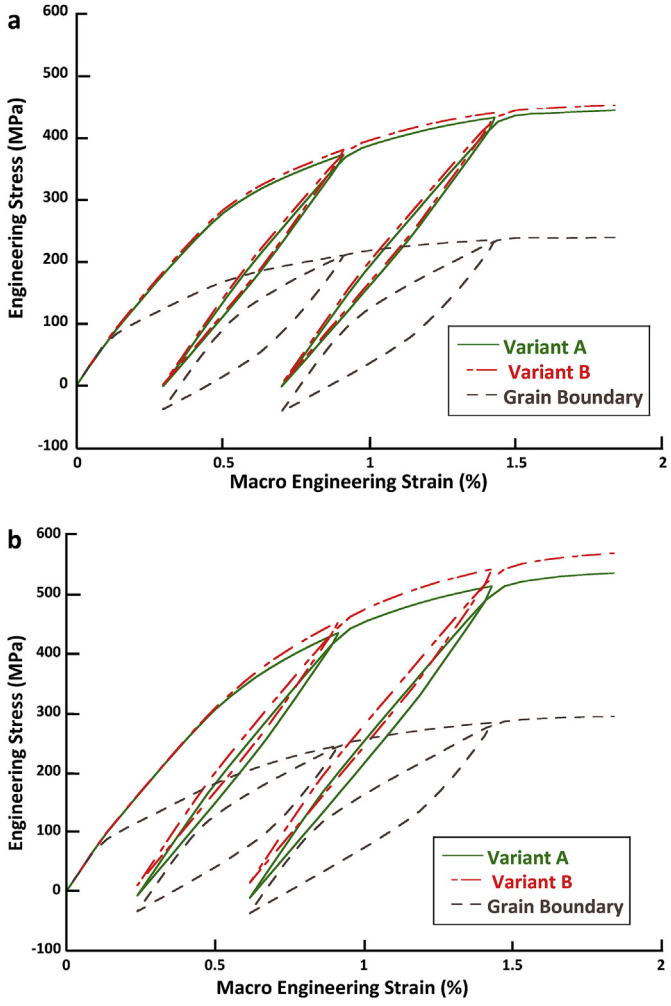

Fig. 13. Volume average of variant (σ_{yy}^{var}) and grain boundary (σ_{yy}^{GB}) stresses versus the macroscopic engineering strain (ε_{yy}) from simulations of quasi-static cyclic loading parallel to (a) the [001] direction in Variant A and (b) the $[1\bar{1}2]$ direction in Variant A.

could be modeled using a rate sensitive mechanism, thereby providing a link between grain rotations and the rate sensitive response. The model proposed here can indeed be used to look into this aspect, by assigning a viscoplastic response to the GB phase and recalibrating and validating all material constants. Then, rotation of the lattice produced by this process could be tracked by the rotation component of the elastic part of the deformation gradient, given that a multiplicative decomposition was used here, and then mapping appropriate lattice vectors using that component to keep track of the grain orientation. This work is in progress and will be reported elsewhere.

A good starting point would be to assume that the strain rate sensitivity of the GBs is similar to that of grain interiors. Under this assumption, the strain concentrations at the boundaries would likely lead to higher overall flow stresses due to a "notch" effect (higher local strain rates for the same macroscopic applied strain rate), and likely lead to some variation in the calibrated constants for the crystal plasticity model. Nevertheless, these effects are not expected to be large for loading along the $[001]_{G\_A}$ direction, and the use of viscoplasticity for the GB phase might actually lead to more homogeneity in the response for that case since the GB would be stiffer and probably transfer the stresses and strains better across grains of the two variants. This, in turn, might lead to lower values of hardening constants and help decrease the slight over-prediction of the response for the $[1\bar{1}2]_{G\_A}$ case as compared to the experiment. This work is also currently underway and will be reported in future publications.

The strain and stress partitioning is also likely to contribute to the phenomena discussed above. In this regard, it is interesting that the strain in each variant predicted by the simulations can be explained by a simple weighted average based on the Schmid factors. At 1.5% applied strain for loading along $[1\bar{1}2]_{G\_A}$, the strain carried by variant A is about 1.32% and for variant B it is 0.867% (Fig. 12), which leads to $\varepsilon^A_{yy}/\varepsilon^B_{yy} = 1.32/0.867 = 1.52$. Note that this is nearly identical to the ratio of the Schmid factors for these two variants (0.408/0.272 = 1.5.). The presence of curvature in these plots (Fig. 12) shows that the behavior changes as a function of applied strain. Specifically, the ratio of the strains in the two variants starts at less than 1.5 (close to 1 till ~0.2% strain and ~1.22 at 0.75% strain), which should be expected due to the presence of the more compliant grain boundary phase that leads to gradual development of strain and stress partitioning between the variants. Nonetheless, the ratio becomes closer to 1.5 for larger strains, which suggests that as plastic strain increases the Schmid factors control the behavior more closely, at least for the range of strains used in the simulations.

The curvature can be explained by the increased hardening in Variant B due to multiple slip along its [111] loading axis, and its higher rate of hardening compared to Variant A, which starts with symmetric double slip. The behavior beyond the 1.5% strain used in the simulations is likely to depend strongly on hardening behavior. If additional curvature developes as a result of further increases in hardening rate in Variant B, then the ratio of the strains carried by the two variants can exceed 1.5, i.e., Variant B carries even less strain. However, if the hardening saturates and the hardening rate becomes low for both variants, then the ratio of their strains is likely to stay the same. The overall stress-strain behavior shown in Fig. 9 suggests that the hardening rate is approaching saturation as the slope of the curves is reaching low values at 1.5% strain.

The way the strain partitions indicates that neither the Taylor (isostrain) or Sachs (isostress) [46] assumptions apply in this case, so the variants are in a "compliant" loading state. Nonetheless, the strain portioning seems to be controlled by the Schmid factor, as pointed out above. Further simulations will be conducted to study these effects in more detail. It is also worth pointing out that the partitioning of strain *between* the grain variants (families) in our UFG Al films, as revealed by the simulations, is in stark contrast to the behavior of NC metals. In NC metals, stress/strain redistribution occurs primarily *within* grain families at small plastic strains (<2%) due to the presence of plastically "soft" and "hard" grains [29]. Capturing these stress redistributions in NC metals requires the use of quantized crystal plasticity models, where a wide, asymmetric distribution of critical resolved shear stresses is assumed for the grains [29], [32].

4.2. Hysteresis of stress-strain response

The hysteresis in the stress-strain response of the bicrystalline films (Fig. 7b) is essentially a consequence of the inelastic stress-strain response during unloading, sometimes referred to as the early Bauschinger effect (BE). BE in UFG metals has been attributed to inhomogeneous stress distribution caused by microstructural heterogeneity [28], which leads to reverse yielding of plastically soft grains during unloading [47]. While there are many possible sources of heterogeneity, the distribution in size and orientation of grains is particularly important. The effect of grain size distribution manifests as a variation in yield strength (critical resolved shear stress) of different grains, whereas the orientation dictates the resolved shear stress acting on the grains through the Schmid factor for each variant. In simulations used in this work, a grain boundary region was used and found to be key to model the stress-strain response, particularly given that the almost bicontinuous distribution of the two variants (see Fig. 2) makes it hard to quantify what the grain size variability really is for the samples tested here. However, note that the effects of the grain boundary region and local grain size are likely correlated, since smaller grains will have a larger fraction of grain boundary region. For the bicrystalline Al films explored in this study, loading along $[001]_{G\_A}$ minimizes the variation of the resolved shear stress (low plastic heterogeneity). As a result, the stress-strain hysteresis observed for $[001]_{G\_A}$ loading is likely to result mainly from the grain size and grain boundary effects. In contrast, for $[1\bar{1}2]_{G\_A}$ loading both the grain size variation and heterogeneity in plastic behavior due to anisotropy are likely contribute to the hysteresis. In particular, note that for cyclic loading along $[1\bar{1}2]_{G\_A}$ (Fig. 13b) not only the stresses for the grain boundary phase become negative when unloading is complete, but also the stresses in variant B do so, which does not occur for loading along the $[001]_{G\_A}$. This is clear evidence that additional back-stresses develop in this case, which strongly suggests that the difference in hysteresis between the two loading directions is also directly affected by the heterogeneity in the plastic behavior induced by anisotropy.

It is important to point that despite the useful insights provided by the model used here, it still had some limitations while trying to match quantitatively the quasi-static cyclic behavior for loading along $[1\bar{1}2]_{G\_A}$. In particular, the model overpredicted the overall flow stress measured during the experiment, by a slightly larger margin than that for the monotonic case shown in Fig. 9, and also underestimated the values of the hysteresis strain ε_h as a function of applied strain. Some preliminary modifications to the model indicate that a higher compliance of the grain boundary region for loading along $[1\bar{1}2]_{G\_A}$ would correct for some of these effects. This suggests, given the good match obtained from loading along along $[001]_{G\_A}$, that the properties of the grain boundary region are likely to be anisotropic as well, as they need to change with loading direction. Furthermore, and perhaps more importantly, there are likely additional deformation mechanisms with higher strain rate sensitivity than those suggested by values of m shown in Fig. 6c. In

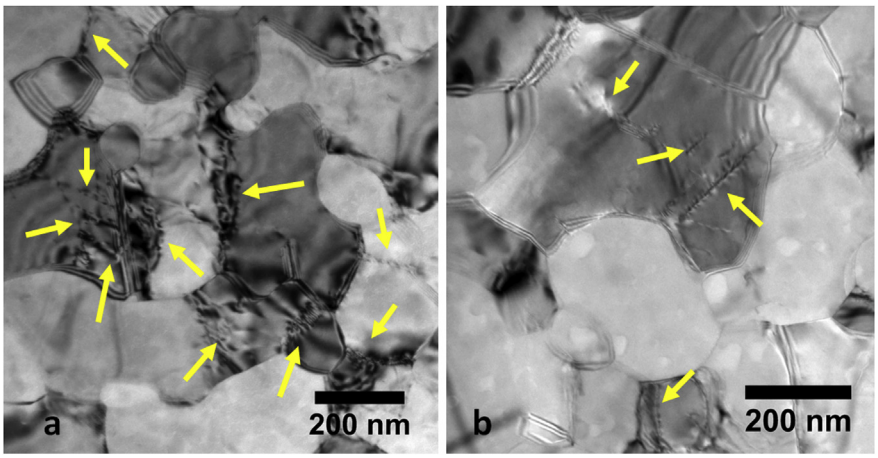

Fig. 14. (a) Bright-field TEM image of numerous dislocation entanglements, indicated by yellow arrows, in the 180 nm film after loading along $[001]_{G\_A}$ direction. (b) Bright-field TEM image of dislocation entanglements in the 180 nm film after loading along $[1\bar{1}2]_{G\_A}$ direction. Fewer dislocation entanglements were seen in this case. Both samples were deformed to the same strain (~0.9%). (For interpretation of the references to colour in this figure legend, the reader is referred to the web version of this article.)

particular, note from Fig. 7b that the unloading locations for the data obtained along $[1\bar{1}2]_{G\_A}$ show evidence of stress relaxation behavior (actuator displacement was held constant for 1–2 min before unloading began). The presence of viscoplasticity can introduce additional strains that can lead to increased compliance. The use of a viscoplastic model for the grain boundary region, as suggested in Ref. [39] and references therein and also as discussed above is a way to take this into account and likely to produce an even better quantitative matching of the observed behavior.

4.3. Strain hardening

As discussed in section 3.2, both the stress-strain response during the first loading and the residual strain hardening in the subsequent cycles was dependent on the loading direction. Since the $[001]_{G\_A}$ loading leads to a relatively high Schmid factor in all the grains, yielding occurs earlier compared to the $[1\bar{1}2]_{G\_A}$ loading direction and the stresses are lower. However, because many slip systems are simultaneously activated, there is a higher probability of dislocation entanglements. As a result, there is significant residual hardening in the subsequent cycles. Qualitative post-mortem TEM observations indeed reveal significant residual dislocation networks as shown in Fig. 14a. The opposite case applies for the $[1\bar{1}2]_{G\_A}$ loading. The yield stress during the first cycle is high because of the low Schmid factor ($s = 0.272$) of one of the grain variants. But because only two slip systems are activated in the plastically soft grain variant ($s = 0.408$), dislocation entanglements are less likely (Fig. 14b) and lead to smaller residual hardening. This also justifies the choice of hardening law for the crystal plasticity modeling of grain interiors, as Asaro's model is indeed based on the assumption that dislocations can be stored, and interact to produce hardening.

5. Conclusions

In this study, we have explored the effect of plastic anisotropy on the deformation behavior of UFG aluminum films with a bicrystalline texture. By systematically choosing two loading directions that minimized/maximized the heterogeneity due to texture-induced plastic anisotropy, we have shown that plastic anisotropy influences the flow stress, strain rate sensitivity, Bauschinger effect and residual hardening of UFG films. Thus, these results strongly imply that apart from the mean grain size and distribution, crystallographic texture needs to be taken into account for understanding and predicting the deformation behavior of UFG metals.

In addition, using microstructurally explicit finite element simulations based on crystal plasticity we have shown that strain portioning in the grains follows the Schmid rule and neither isostress nor isostrain assumptions hold for the deformation of these films. The good correspondence between the simulations and experiments of the overall stress-strain behavior also indicates that conventional crystal plasticity, used in a composite model with a grain boundary phase to model the compliance of the interfaces, is adequate to describe the behavior of UFG metals. This observation contrasts with NC metals, for which quantized crystal plasticity models [29,31], that incorporate discrete strain bursts and a distribution of grain-level yield stresses are required to replicate the stress-strain response.

Acknowledgements

This material is based upon work supported by the National Science Foundation under awards CMMI 1400505 and DMR 1454109. The authors would like to gratefully acknowledge the use of facilities at the John M. Cowley Centre for High Resolution Electron Microscopy and the Centre for Solid State Electronics Research at Arizona State University.

References

[1] M.A. Meyers, A. Mishra, D.J. Benson, Mechanical properties of nanocrystalline materials, Prog. Mater. Sci. 51 (4) (May 2006) 427–556.
[2] J.C.M. Li, Mechanical Properties of Nanocrystalline Materials, CRC Press, 2011.
[3] R.Z. Valiev, Y. Estrin, Z. Horita, T.G. Langdon, M.J. Zehetbauer, Y. Zhu, Producing bulk ultrafine-grained materials by severe plastic deformation: ten years later, JOM 68 (4) (Feb. 2016) 1216–1226.
[4] I.P. Semenova, A.V. Polyakov, G.I. Raab, T.C. Lowe, R.Z. Valiev, Enhanced fatigue properties of ultrafine-grained Ti rods processed by ECAP-conform, J. Mater. Sci. 47 (22) (Jul. 2012) 7777–7781.
[5] Z. Horita, M. Furukawa, M. Nemoto, A.J. Barnes, T.G. Langdon, Superplastic forming at high strain rates after severe plastic deformation, Acta Mater. 48 (14) (Sep. 2000) 3633–3640.
[6] H.S. Kim, S.J. Yoo, J.W. Ahn, D.H. Kim, W.J. Kim, Ultrafine grained titanium sheets with high strength and high corrosion resistance, Mater. Sci. Eng. A 528 (29–30) (Nov. 2011) 8479–8485.
[7] J. Rajagopalan, C. Rentenberger, H. Peter Karnthaler, G. Dehm, M.T.A. Saif, In situ TEM study of microplasticity and Bauschinger effect in nanocrystalline metals, Acta Mater. 58 (14) (Aug. 2010) 4772–4782.
[8] R. Schwaiger, B. Moser, M. Dao, N. Chollacoop, S. Suresh, Some critical experiments on the strain-rate sensitivity of nanocrystalline nickel, Acta Mater. 51 (17) (Oct. 2003) 5159–5172.

[9] Y.M. Wang, A.V. Hamza, E. Ma, Temperature-dependent strain rate sensitivity and activation volume of nanocrystalline Ni, Acta Mater. 54 (10) (Jun. 2006) 2715–2726.
[10] Z. Jiang, X. Liu, G. Li, Q. Jiang, J. Lian, Strain rate sensitivity of a nanocrystalline Cu synthesized by electric brush plating, Appl. Phys. Lett. 88 (14) (2006), 143115.
[11] Y.M. Wang, E. Ma, Strain hardening, strain rate sensitivity, and ductility of nanostructured metals, Mater. Sci. Eng. A 375–377 (Jul. 2004) 46–52.
[12] K. Jonnalagadda, N. Karanjgaokar, I. Chasiotis, J. Chee, D. Peroulis, Strain rate sensitivity of nanocrystalline Au films at room temperature, Acta Mater. 58 (14) (Aug. 2010) 4674–4684.
[13] H.S. Kim, Y. Estrin, Phase mixture modeling of the strain rate dependent mechanical behavior of nanostructured materials, Acta Mater. 53 (3) (Feb. 2005) 765–772.
[14] E.O. Hall, The deformation and ageing of mild steel: III discussion of results, Proc. Phys. Soc. B 64 (Sep. 1951) 747–753.
[15] N.J. Petch, The cleavage strength of polycrystals, J. Iron Steel Inst. 174 (8) (1953) 25.
[16] S.S. Shishvan, E. Van der Giessen, Distribution of dislocation source length and the size dependent yield strength in freestanding thin films, J. Mech. Phys. Solids 58 (5) (May 2010) 678–695.
[17] H.D. Espinosa, B.C. Prorok, B. Peng, Plasticity size effects in free-standing submicron polycrystalline FCC films subjected to pure tension, J. Mech. Phys. Solids 52 (3) (Mar. 2004) 667–689.
[18] L. Nicola, E.V. der Giessen, A. Needleman, Discrete dislocation analysis of size effects in thin films, J. Appl. Phys. 93 (10) (May 2003) 5920–5928.
[19] L.B. Freund, The stability of a dislocation threading a strained layer on a substrate, J. Appl. Mech. 54 (3) (Sep. 1987) 553–557.
[20] W.D. Nix, Yielding and strain hardening of thin metal films on substrates, Scr. Mater. 39 (4) (1998) 545–554.
[21] W.D. Nix, O.S. Leung, Thin films: plasticity, Encycl. Mater. Sci. Technol. (2001) 9262.
[22] T. Chookajorn, H.A. Murdoch, C.A. Schuh, Design of stable nanocrystalline alloys, Science 337 (6097) (Aug. 2012) 951–954.
[23] S. Zheng, et al., High-strength and thermally stable bulk nanolayered composites due to twin-induced interfaces, Nat. Commun. 4 (Apr. 2013) 1696.
[24] R.A. Andrievski, Review of thermal stability of nanomaterials, J. Mater. Sci. 49 (4) (Nov. 2013) 1449–1460.
[25] V. Borovikov, M.I. Mendelev, A.H. King, R. LeSar, Effects of Schmid factor and slip nucleation on deformation mechanism in columnar-grained nanotwinned Ag and Cu, J. Appl. Phys. 117 (8) (Feb. 2015), 085302.
[26] F. Dalla Torre, H. Van Swygenhoven, M. Victoria, Nanocrystalline electrodeposited Ni: microstructure and tensile properties, Acta Mater. 50 (15) (2002) 3957–3970.
[27] E. Izadi, J. Rajagopalan, Texture dependent strain rate sensitivity of ultrafine-grained aluminum films, Scr. Mater. 114 (Mar. 2016) 65–69.
[28] J. Rajagopalan, M.T.A. Saif, Effect of microstructural heterogeneity on the mechanical behavior of nanocrystalline metal films, J. Mater. Res. 26 (22) (Nov. 2011) 2826–2832.
[29] L. Li, S. Van Petegem, H. Van Swygenhoven, P.M. Anderson, Slip-induced intergranular stress redistribution in nanocrystalline Ni, Acta Mater. 60 (20) (Dec. 2012) 7001–7010.
[30] M. Haouaoui, I. Karaman, H.J. Maier, Flow stress anisotropy and Bauschinger effect in ultrafine grained copper, Acta Mater. 54 (20) (2006) 5477–5488.
[31] L. Li, M.-G. Lee, P.M. Anderson, Critical strengths for slip events in nanocrystalline metals: predictions of quantized crystal plasticity simulations, Metall. Mater. Trans. A 42 (13) (Sep. 2010) 3875–3882.
[32] P.M.A. Lin Li, The stress–strain response of nanocrystalline metals: a quantized crystal plasticity approach, Acta Mater. 57 (3) (2009) 812–822.
[33] H. Niwa, M. Kato, Epitaxial growth of Al on Si(001) by sputtering, Appl. Phys. Lett. 59 (5) (1991) 543.
[34] J.H. Han, M.T.A. Saif, In situ microtensile stage for electromechanical characterization of nanoscale freestanding films, Rev. Sci. Instrum. 77 (4) (2006), 045102.
[35] G. Simmons, H. Wang, Single Crystal Elastic Constants and Calculated Aggregate Properties. A Handbook, second ed., The MIT Press, Cambridge, Mass, 1971.
[36] R.J. Asaro, Micromechanics of crystals and polycrystals, Adv. Appl. Mech. 23 (Jan. 1983) 1–115.
[37] C.-H. Goh, D.L. McDowell, R.W. Neu, Plasticity in polycrystalline fretting fatigue contacts, J. Mech. Phys. Solids 54 (2) (Feb. 2006) 340–367.
[38] E.B. Marin, On the Formulation of a Crystal Plasticity Model, SAND2006–4170, Sandia National Laboratories, Aug. 2006.
[39] L. Mishnaevsky, E. Levashov, Micromechanical modelling of nanocrystalline and ultrafine grained metals: a short overview, Comput. Mater. Sci. 96 (2015) 365–373.
[40] L. Stéphane, B. Stéphane, Une Toolbox Abaqus pour le calcul de propriétés effectives de milieux hétérogènes, in Une Toolbox Abaqus pour le calcul de propriétés effectives de milieux hétérogènes, Giens, France, 2011.
[41] J.F. Thomas, Third-order elastic constants of aluminum, Phys. Rev. 175 (3) (Nov. 1968) 955–962.
[42] W.D. Nix, Yielding and strain hardening of thin metal films on substrates, Scr. Mater. 39 (4) (1998) 545–554.
[43] L.B. Freund, W.D. Nix, A critical thickness condition for a strained compliant substrate/epitaxial film system, Appl. Phys. Lett. 69 (2) (Jul. 1996) 173–175.
[44] C. Zhou, R. LeSar, Dislocation dynamics simulations of plasticity in polycrystalline thin films, Int. J. Plast. 30–31 (Mar. 2012) 185–201.
[45] E. Izadi, A. Darbal, R. Sarkar, J. Rajagopalan, Grain rotations in ultrafine-grained aluminum films studied using in situ TEM straining with automated crystal orientation mapping, Mater. Des. 113 (Jan. 2017) 186–194.
[46] U.F. Kocks, The relation between polycrystal deformation and single-crystal deformation, Metall. Mater. Trans. 1 (5) (May 1970) 1121–1143.
[47] J. Rajagopalan, J.H. Han, M.T.A. Saif, Bauschinger effect in unpassivated freestanding nanoscale metal films, Scr. Mater. 59 (7) (Oct. 2008) 734–737.